



Monitoring the vertical changes of a tidal flat using a MEMS accelerometer array

Chunying Xu^{a,b,c,d,*}, Jiawang Chen^b, Yongqiang Ge^b, Ziqiang Ren^b, Chen Cao^b, Hai Zhu^b, Yue Huang^b, Hao Wang^b, Wei Wang^b

^a College of Engineering, Shantou University, 515013, China

^b Ocean collage, Zhejiang University, Zhoushan, 316021, China

^c Key Laboratory of Intelligent Manufacturing Technology (Shantou University), Ministry of Education, Shantou, China, 515013

^d Guangdong Provincial Key Laboratory of Digital Signal and Image Processing, Shantou, Shantou, China, 515013

ARTICLE INFO

Keywords:

Tidal flat
Non-uniform sampling
Equal arc length sampling
Two-dimensional arc model
Vertical change
Wave period
Micro-Electro-Mechanical System
accelerometer array

ABSTRACT

Tidal flats are constantly affected by the tide and are alternately exposed and submerged. Therefore, it is very difficult to monitor their topographic vertical changes (subsidence or uplifting) as the geographical environment is unique. In this study, a monitoring system based on the Micro-Electro-Mechanical System (MEMS) accelerometer array is proposed for monitoring subsidence or uplift in tidal flats. The optimal arrangement of the MEMS accelerometer array was determined using the non-uniform sampling theorem (frame theory) and the amplitude distribution characteristics of the tidal flat, and was as follows: the arc length interval between the sensors should be less than double the highest frequency of the tidal flat which is a baseband signal. We theoretically proved that the MEMS accelerometer array which satisfies the requirement of the non-uniform sampling with equal arc length could completely reconstruct the tidal flat. The two-dimensional arc model for reconstructing the tidal flat was then presented. To validate and correct the non-uniform sampling conditions obtained, and the calculation model, a test was conducted on a tidal flat in Zhairuoshan Island. The wave period and the vertical change of the tidal flat are measured. The results demonstrate the feasibility of the proposed system for effective tidal flat monitoring.

1. Introduction

Tidal flats are areas between the mean higher high water and mean lower low water lines, which also known as the intertidal zones [1]. Tidal flats occupy approximately 7% of the total coastal shelf areas worldwide [2,3], and are an important sedimentary zone conjoining the land and sea. They provide benefits to humans, such as defense against storm surges and flooding, and productive habitats for fish and migratory birds [4–7]. Shaped by tides, waves, and other sedimentary factors, the topography of tidal flats is highly dynamic over time and space [8]. The topographic vertical changes of tidal flats are complex, including sediment deposition or erosion and consolidation or expansion induced by soil. It is important to monitor the topographic vertical changes of tidal flats in coastal management, sea-level change research, environmental protection, and sustainable coastal development [9]. Thus, vertical changes in tidal flats or intertidal areas, have attracted worldwide interest [10].

It is difficult to monitor the topography of tidal flats as they are

alternately exposed at low-tide and submerged at high-tide, and access to such sites is limited [11]. The monitoring of tidal flats is also laborious due to the great morphological changes caused by ocean tides, currents, and river flows in estuaries. Owing to these limitations, there have been few investigations and comprehensive reports focusing on tidal flats [4]. Approaches commonly used for mapping coastal bathymetry include satellite remote-sensing [4,12–15], airborne Light Detection and Ranging (LiDAR) [16–19], ship-based single/multi-beam echo sounding [2,20], waterline method [21–23], Rod surface elevation tables (RSETs) [24–26], and Terrestrial laser scanners (TLS) [27,28]. Satellite remote-sensing is a major tool for monitoring topographic changes [29]. The most common remote sensing approach to assessing topographic change involves visual interpretation, which has inherent issues because it is subjective, in most cases [30,31]. Many factors could influence the monitoring accuracy, including the tidal stage, beach slope, position of the groundwater exit point, and the viewing geometry of the sensor [29,30]. The LiDAR and interferometric synthetic aperture radar (In-SAR) systems are other remote-sensing techniques for

* Corresponding author at: Shantou University, 515013, China.

E-mail addresses: chunyingxu@stu.edu.cn, chunyingxu@zju.edu.cn (C. Xu).

<https://doi.org/10.1016/j.apor.2020.102186>

Received 1 October 2019; Received in revised form 16 March 2020; Accepted 27 April 2020

Available online 09 June 2020

0141-1187/ © 2020 Elsevier Ltd. All rights reserved.

measuring the topography tidal flats [11,15,19]. The accuracy of digital elevation models (DEMs) is several centimeters, with occasional deviations to 20 cm, when using LiDAR or acoustic methods [4,32]. The RSETs is based on a nine-point grid within a small area attached to a single arm connected to a vertical pipe, which is introduced into another pipe permanently installed in the sediment. The arm can rotate. Thus, accurate measurements can be obtained in a circle around the central pipe. Although the RSETs allows very precise measurements to within 1.5 mm [33] that can be regularly taken, construction and implementation costs is expensive, especially if the study covers a wide area with large point density. A system that can overcome these limitations is required for monitoring the real-time subsidence of tidal flats with high accuracy. A monitoring method based on the (Micro-Electro-Mechanical System) MEMS sensor could resolve these issues in the study of tidal flats [34–37].

The main purpose of this study was to determine the optimal arrangement of a MEMS sensor array and test its ability to monitor tidal flats. A one-dimensional non-uniform sampling theorem is introduced, and the data for a tidal flat in Zhairuoshan Island are then collected, and their amplitude distribution is analyzed by one-dimensional Fourier transform analysis. The relationship between the one-dimensional non-uniform sampling theorem and the arrangement conditions of the MEMS sensor array is also described. The approach for calculating the topographic vertical changes of the tidal flat is then described. To validate the optimal arrangement conditions obtained and the calculation of the topographic changes of the tidal flat, a test was conducted for a tidal flat in Zhairuoshan Island. Finally, the conclusion is presented.

2. Study area

Zhairuoshan island (29°56' N, 122°5' E) is located in the middle of China Zhoushan fishing ground in Zhejiang, China, as shown in Fig. 1. Zhairuoshan island is 4.8 km away from Zhoushan island. The coastline is 7.27 km long and covers an area of 2.7 km², of which the land area is 2.34 km² and the tidal flat is 0.36 km². There are three tidal flats in the east, west, and north on the Zheshan Island. Each tidal flat is surrounded by mountains on three sides and one facing the sea.

Zhairuoshan Island is an experimental island for Zhejiang University. The natural experimental conditions on the Zhairuoshan Island are very good. The seawater around Zhairuoshan Island contains a lot of sediment, and the sedimentation amount is very large. The topographic vertical changes of the tidal flat in Zhairuoshan Island include sediment deposition or erosion, as well as soil consolidation and expansion. However, research on topographic vertical changes in tidal flat on the Zhairuoshan Island has never been reported before.

3. One-dimensional non-uniform sampling theorem, arrangement conditions of the MEMS sensor array and two-dimensional arc reconstruction algorithm

The MEMS accelerometers were arranged in an array with equal arc length intervals. When the tidal flat was flat, the sensors were evenly spaced at equal intervals. The sampling points were also evenly spaced (uniform sampling). The sensor array changed when the tidal flat deformed. The arc length between the sensors was a fixed value, thus, the sampling points were not evenly spaced (non-uniform sampling), as shown in Fig. 2. That is, the sensor array shifted from uniform sampling to non-uniform sampling when the tidal flat deformed from flat to uneven. In this study, the non-uniform sampling method with an equal arc length has an "adaptive" capability: on the rough tidal flat, the sampling intervals were smaller and there were more sampling points, and, on the flat areas, the sampling intervals were larger and there were fewer sampling points.

The Shannon sampling theorem [39] was followed for uniform sampling. The non-uniform sampling approach was not random or

arbitrary. Therefore, it was necessary to theoretically verify whether the non-uniform sampling method in this study could monitor the tidal flat without distortion. Detailed derivation processes of the one-dimensional non-uniform sampling theorem are in the Appendix A.

The tidal flat in Zhairuoshan Island was surveyed. A three-dimensional (3D) laser scanning system (Scanstation P40, Leica Geosystems, Switzerland) was used to collect data, and included 3D laser scanners, mobile power supplies, dedicated targets, dedicated tripods, and data-processing software. The accuracy of this system is 3 mm at 50 m. The survey area is 16 × 8 m, as shown in Fig. 3. The amplitude range of the survey area was −0.17 to 0.43 m.

The tidal flat data were extracted from the 3D laser scanning software at intervals of 0.1 m in the x-direction at y = 0.5 m, 1 m, ... to 8 m (interval of 0.5 m). A total of 160 samples were collected in the x-axis direction.

The one-dimensional discrete Fourier transformation of the tidal flat in Zhairuoshan island was calculated, and its amplitude was obtained (Detailed derivation processes are in the Appendix B). The arrangement conditions of the sensor array were also obtained (Detailed derivation processes are in the Appendix C).

To monitor the topographic vertical changes of the tidal flat, its shapes should first be reconstructed. The amount of the subsidence and uplifting can then be obtained from the time series of the tidal flat. The shape of the tidal flat (strip shape) could be approximated using curves measured by the sensor array. The detailed derivation process of two-dimensional arc reconstruction algorithm is in the Appendix D.

4. Tidal flat monitoring experiment

Fig. 4 shows a schematic diagram of the subsidence monitoring of the tidal flat, while Fig. 5 presents a diagram of the deployment of the sensor array. The sensor array was fixed to the tidal flat terrain on a net with pilings, where piling 1 serves as the reference point of the sensor array, and the sensor array was arranged perpendicular to the embankment. There was a ruler on the PVC tube which can provide measurement with an accuracy of 0.1 cm. The sensors were placed every 30 cm on the array, and a total of seven sensors were arranged with a total length of 2.1 m. As mentioned in the Appendix C, the interval between the sensors was smaller than $\frac{1}{2\Omega} \approx 1.33$ m, and the shapes of the tidal flat could be completely reconstructed. The tidal flat could be monitored without distortion, as 30 cm is much smaller than 1.33 m. In this experiment, the sensor array measured and collected data every 100 ms. The data was processed and reconstructed using the two-dimensional arc model presented in the Appendix D. The shape of the sensor array could then be compared with the data from the 3D laser scanner, which only collected data after the tide ebbed.

5. Experiment result

The sensor array was deployed from October 25–27, 2018. The data from the sensor array when the array was exposed were collected on October 25–26, while the data when tidewater reached and left the sensor array were collected on October 26–27. The 3D laser scanner was operated when the tidewater was ebbed and the sensor array was exposed to the air. The data obtained from the sensor array and 3D laser scanner were compared. Fig. 6 shows the tidal flat and sensor array obtained from the commercial software of the 3D laser scanner (Cy-clone).

5.1. Changes in the pitch angle during high and low tides

As sensors #6 and #7 failed, data from these sensors were not returned. Therefore, sensor array data were only collected from sensors #1 to #5. Fig. 7 presents the rotation angle of sensor #3 around the y-axis (pitch angle) from October 26 to 27. The blue curve is the original data, and the red curve was filtered by the moving average.

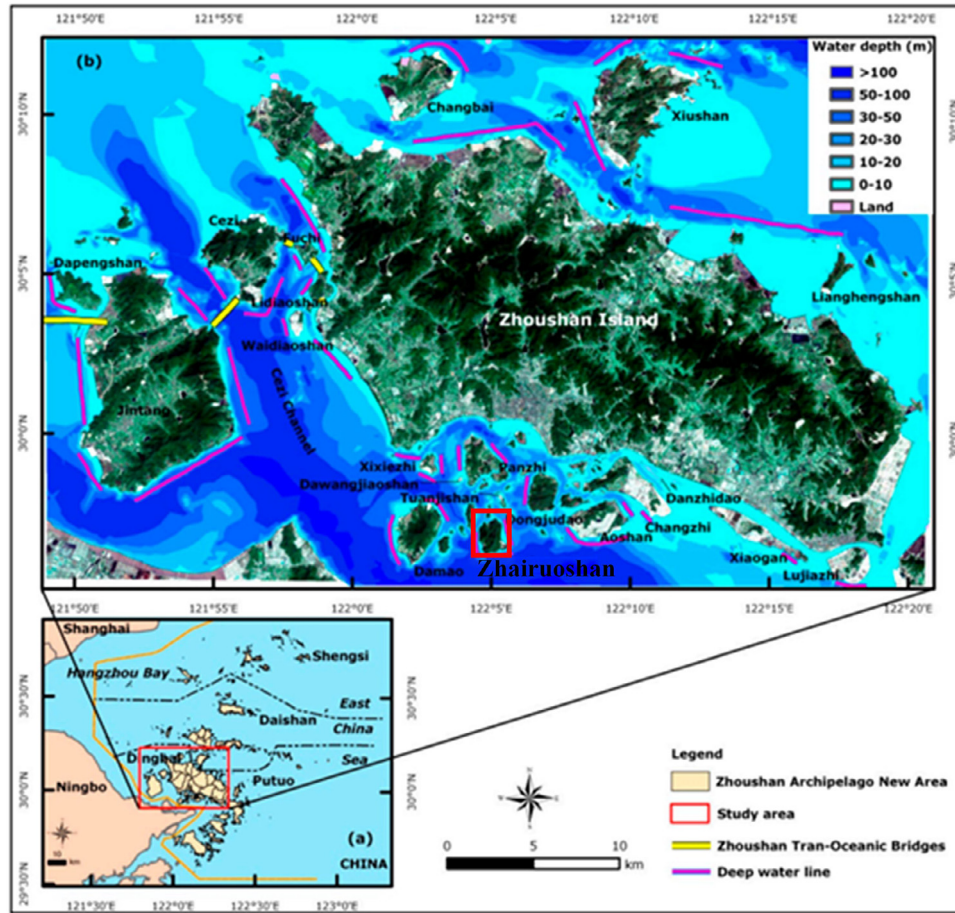


Fig. 1. the location of the Zhairuoshan island in Zhoushan island, China modified from [38].

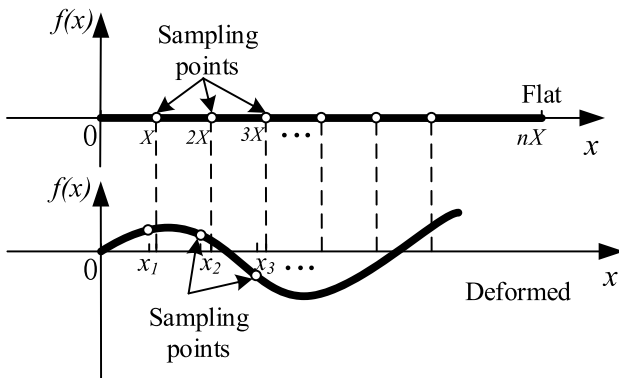


Fig. 2. One-dimensional non-uniform sampling with equal arc length.

Fig. 7 shows that the data from the sensor array differed between tidal ebb and flow. The variations in the data when the sensor array was submerged in tidewater or exposed were small. Before the tide reached the sensor array (20:24 on October 26), the pitch angle of sensor #3 was -0.255° (average), indicating that it was relatively stable. After the tide reached the sensor array (20:24 on October 26), the angle changed to 0.856° (average). After the tide left the sensor array at 01:18 on October 27, the angle was -0.519° . At the next high and low tides (from 08:33 to 13:59 on October 27), the angle changed in the same manner.

The green box in Fig. 7 indicates the changes in the data from sensor #3 during the arrival of a tide. To further understand these changes, Fig. 8 shows a partial enlargement of the changes during the arrival of high and low tide. As shown in Fig. 8(a), during the arrival of high tide, it took approximately seven minutes for the tide to fully submerge the sensor. The sensor was sometimes submerged by the tidewater and sometimes exposed. In the process, the values of the sensor will have

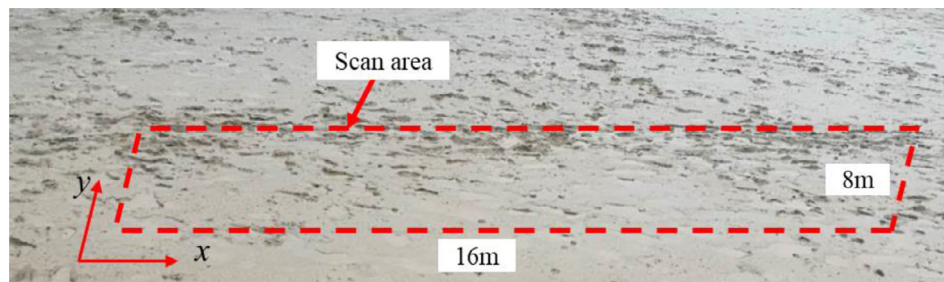


Fig. 3. Surveyed tidal flat area in Zhairuoshan Island.

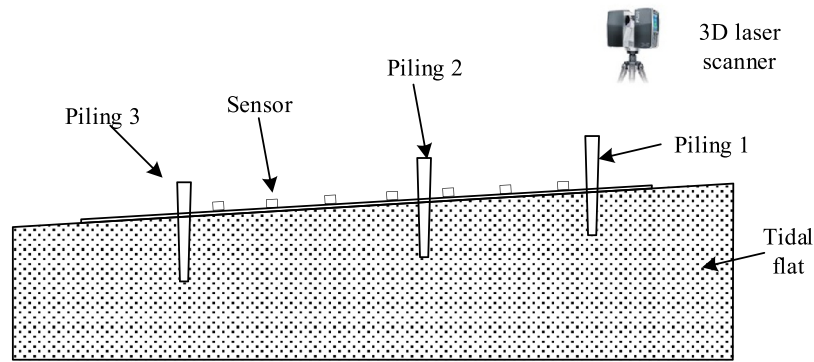


Fig. 4. Schematic diagram of the tidal flat monitoring experimental setup.

jumps when the tide is coming. The difference between the peaks is the time interval of the two waves. The average period of the wave in the high tide is 6.0 s. The range of jitter in the first two minutes was -0.22° to 0.23° , and that in the subsequent five minutes was 0.10° to 1.2° . The angle then tended to stabilize at 0.856° . According to Fig. 8(b), it took approximately three minutes for the tidewater to completely expose the sensor. In the process, the values of the sensor will drop when the tide recedes from the sensor. The difference between the peaks is also the time interval of the two waves. The average period of the wave in the low tide is 9.2 s. During the low tide process, the change in the angle of the sensor was opposite to that during the arrival of high tide. During the first two minutes, the jitter range was larger than during the final minute.

The pitch angle increased and decreased during the arrival of high and low tide, respectively. The jitter range of the pitch angle was larger than that when the sensor array was submerged by tidewater or fully exposed. This is because the sensor array was not completely fixed to the tidal flat.

5.2. Change in the data collected from the sensor array during high and low tide

Fig. 9 shows the change in the data collected from the sensor array during the arrival of high and low tide, and the curves are the average values. The coordinates obtained by the sensor array were relative to the origin, therefore, the changes in the coordinates of the origin should be considered. In this study, the vertical distance change of the start point of the sensor array and highest point of the polyvinyl chloride (PVC) pipe represented the change (subsidence or uplift) of the origin of the sensor array. The change in the coordinates of the origin was measured after the tide ebbed. The vertical distance of the origin of the sensor array from the point of the PVC pipe was 0.27 m at the beginning (06:00–08:00 on October 25), which is the reference vertical distance. The changes in the origin of the sensor array were 0.32 cm (uplift), 0.22 cm (uplift), -0.10 cm (subsidence), and -0.40 cm (subsidence of 0.32 cm) respectively at 14:12, 07:10, 14:30, and 01:18 on October 25,

26, 26, and 27, respectively. The change in the origin could not be measured when it was submerged in tidewater. However, the change in the origin after ebb was small. Therefore, the origin when the sensor array was submerged in tidewater was the same as that when it was exposed. The curves in Fig. 9 also include the change in the origin.

Fig. 9 shows that the curves (blue and pink) of the sensor array when it was submerged in tidewater were higher than those (red, black, and green) when it was exposed. The main reason for this is that the sensor array floats and was not fully fixed to the tidal flat. Additionally, the red, black, and green curves in Fig. 9 do not overlap: the black curve is slightly lower than the red curve (sensor array sinks slightly), and the green curve is higher than the black curve (sensor array rises slightly), indicating that the sensor array was deformed after the high and low tides. As the sensor array floated in the tidewater, the soil under the sensor array was allowed to flow in and out. That is, the sensor array could measure the vertical changes induced by the soil and sediment. Although the sensor array may float in the tide water, it will still fit well on the tidal flat after tide because of the weight of the sensor array and wet net. Thus, the results of the monitoring analysis are reliable.

Table 1 shows the coordinates of the sensor array when it was exposed and the 3D laser scanner from October 25 to 27. The 3D laser scanner could only obtain the precise coordinates of the sensor array when it was exposed. The data in the table are in respect to the change in the origin. That is, they are the relative coordinates with respect to those at the beginning. The table shows that the z-coordinate values of coordinate label 2 obtained from the sensor array and 3D laser scanner differed slightly, while those of the later labels differed greatly. Fig. 10 shows the curves obtained from the sensor array and 3D laser scanner. The same conclusion can be obtained from Fig. 10.

Table 2 shows the coordinate errors between the sensor array and 3D laser scanner. The data obtained by the sensor array differed greatly from those collected by the 3D laser scanner, with a maximum absolute error of 5.53 cm. The maximum root mean square error and mean absolute error were 2.89 and 2.92 cm, respectively. According to the analysis of the differences in the z-coordinate values of two adjacent points (Table 3), the data errors of the second and fourth sensors were



Fig. 5. Deployment of the sensor array.

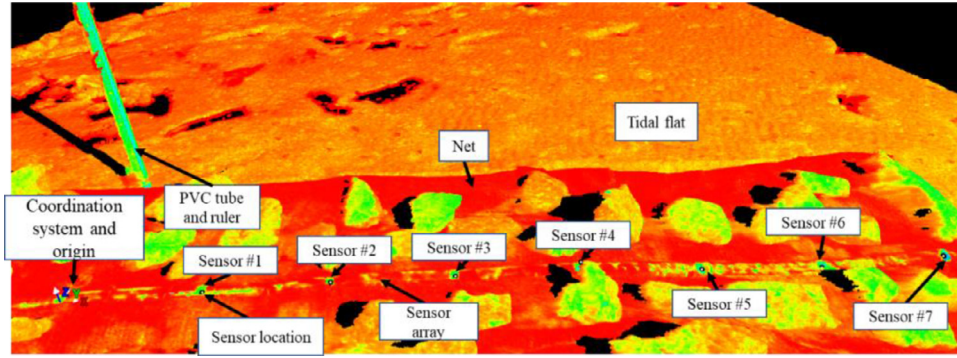


Fig. 6. Sensor array and tidal flat obtained by the 3D laser scanner.

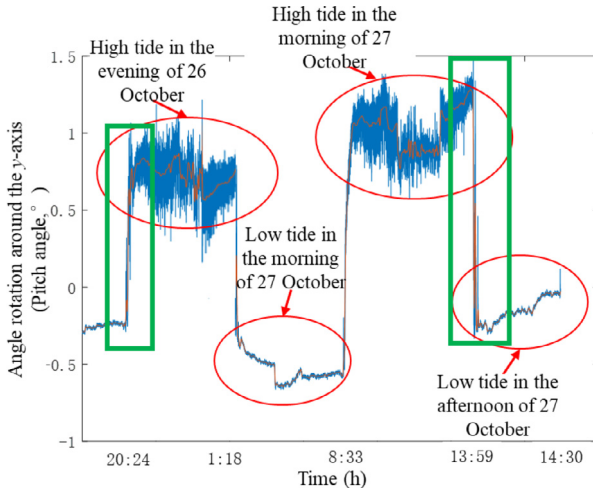


Fig. 7. Changes in the pitch angle (sensor #3) over time.

relatively large, causing the error to accumulate in subsequent points. Further, sensors #2 and #4 were analyzed, and the modulus values of the acceleration of the three axes were 0.9355 and 0.9589, respectively. These values differ from gravitational acceleration (1 g). Therefore, the error of the pitch angle obtained by the two sensors was large, resulting in reconstruction curves that greatly differed from the curves of the 3D laser scanner.

Table 4 shows the coordinate difference errors before and after removing the data of sensors #2 and #4. The errors after removing the failure data from these sensors were much lower. The maximum

absolute error, root mean square error, and mean absolute error before and after removing the failure data were 3.07 and 0.96 cm, 2.15 and 0.95 cm, and 1.19 and 0.52 cm, respectively. As the data obtained using sensors #1, #3, and #5 were relatively accurate, the monitoring was still reliable.

Fig. 11(a) and (b) show the tidal flat levels obtained from the sensor array and 3D laser scanner, respectively, from October 25 to 27 when the sensor array was exposed. The tidal flat uplifted from October 25 to 27. According to Fig. 11 and Table 2, the changes in the coordinates of the tidal flat obtained from the sensor array and 3D scanner were consistent. The mean coordinate change obtained from the sensor array was 1.15 cm, and the maximum coordinate change was 2.22 cm at coordinate label 6. The mean change obtained from the 3D scanner was 1.06 cm, and the maximum coordinate change was 1.91 cm at coordinate label 6. The reconstruction accuracy of the sensor array is significantly higher after the errors are eliminated. In practical application, the sensor will be multi-level calibration before use. In addition, we can judge the correctness of data by checking whether modulus of the triaxial acceleration of the sensor is equal to one. Thus, this monitoring method has great potential in application for tidal flat monitoring with high accuracy.

6. Conclusion

In this study, a monitoring system based on the MEMS accelerometer is presented for monitoring the subsidence or uplifting of tidal flats. The optimal arrangement of the MEMS sensor array was determined by the one-dimensional non-uniform sampling theorem and the amplitude distribution characteristics of the tidal flat. A two-dimensional arc model for reconstructing the tidal was also presented. To

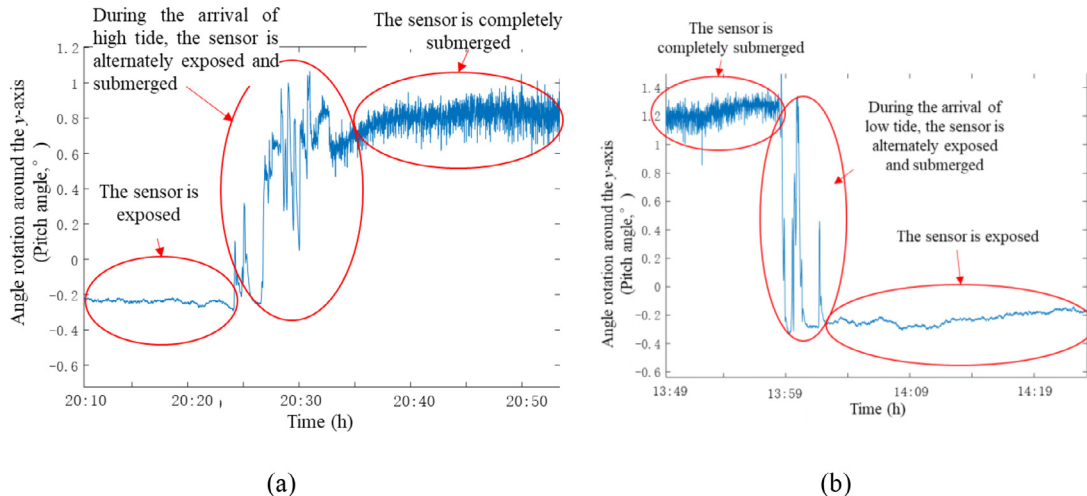


Fig. 8. Partial enlargement in the process of high (a) and low (b) tide.

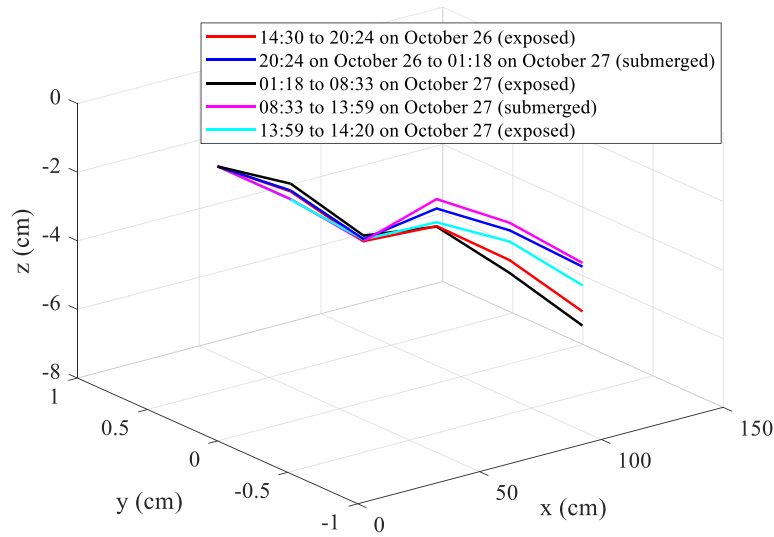


Fig. 9. Changes of the sensor array during the arrival of high and low tides.

validate the arrangement conditions obtained and the calculation principle for reconstructing and monitoring the tidal flat, a test was conducted for a tidal flat in Zhairuoshan Island. The main results of this paper are as follows:

- (1) We can conclude that the one-dimensional relative amplitude spectrum of the tidal flat was concentrated in the low frequency. The highest frequency of the tidal flat was 0.375 m^{-1} .
- (2) According to the derivation of non-uniform sampling theorem, the tidal flat could be completely recovered when the arc length interval between the sensors was less than double the highest

frequency of the tidal flat, which should be less than 1.33 m .

- (3) In the monitoring test of the tidal flat in Zhairuoshan Island, the average period of the wave in the high tide is 6.0 s . The average period of the wave in the low tide is 9.2 s . After removing the error data of sensors #2 and #4, the mean absolute errors are 0.52 cm .

The results show that the novel sensing technique has great potential for real-time tidal flat detection and monitoring applications with high accuracy.

Table 1

Coordinate values obtained from the sensor array and 3D laser scanner when the sensor array was exposed.

Time	Sensor label	Coordinate label	Sensor array (cm)			3D laser scanner (cm)		
			x	y	z	x	y	z
06:00–08:20 on October 25		1	0	0	0	0	0	0
	1	2	29.9	0	−1.634	29.9	0	−0.904
	2	3	59.8	0	−4.38	59.9	0.1	−1.84
	3	4	89.9	0	−4.02	89.9	0.1	−1.59
	4	5	119.8	0	−6.28	119.8	0.2	−1.63
	5	6	149.7	0	−8.49	149.9	0.2	−3.21
14:12–20:03 on October 25	1	2	29.9	0	−1.567	29.9	0	−1.074
	2	3	59.8	0	−4.03	59.9	0.1	−1.95
	3	4	89.8	0	−3.93	89.9	0.2	−1.539
	4	5	119.9	0	−5.38	119.8	0.2	−1.58
	5	6	149.7	0	−8.04	149.8	0.3	−3.50
07:10–08:24 on October 26	1	2	29.9	0	−1.334	29.9	0	−0.86
	2	3	59.8	0	−3.59	59.9	0.1	−1.06
	3	4	89.9	0	−3.97	89.9	0.2	−1.1
	4	5	119.8	0	−5.77	119.9	−0.3	−1.17
	5	6	149.5	0	−7.98	149.8	0.4	−2.88
14:30–20:24 on October 26	1	2	29.9	0	−1.29	29.9	0	−0.8
	2	3	59.8	0	−3.30	59.9	0.1	−0.2
	3	4	89.8	0	−3.34	89.9	0.2	0.0
	4	5	119.6	0	−4.98	119.7	−0.3	−0.2
	5	6	149.7	0	−7.04	149.8	0.4	−1.5
01:18–08:33 on October 27	1	2	29.9	0	−1.06	29.9	0.6	−0.8
	2	3	59.9	0	−3.14	59.9	0.3	0.2
	3	4	89.8	0	−3.44	89.9	−0.2	0.4
	4	5	119.8	0	−5.35	119.8	−0.5	−0.4
	5	6	149.2	0	−7.45	149.4	−0.1	−2.3
13:59–14:30 on October 27	1	2	29.9	0	−1.23	29.9	0.1	−0.7
	2	3	59.9	0	−3.25	59.9	−0.1	−0.1
	3	4	89.9	0	−3.31	89.9	−0.1	−0.1
	4	5	119.8	0	−4.44	119.9	−0.1	0.2
	5	6	149.8	0	−6.27	149.9	−0.6	−1.3

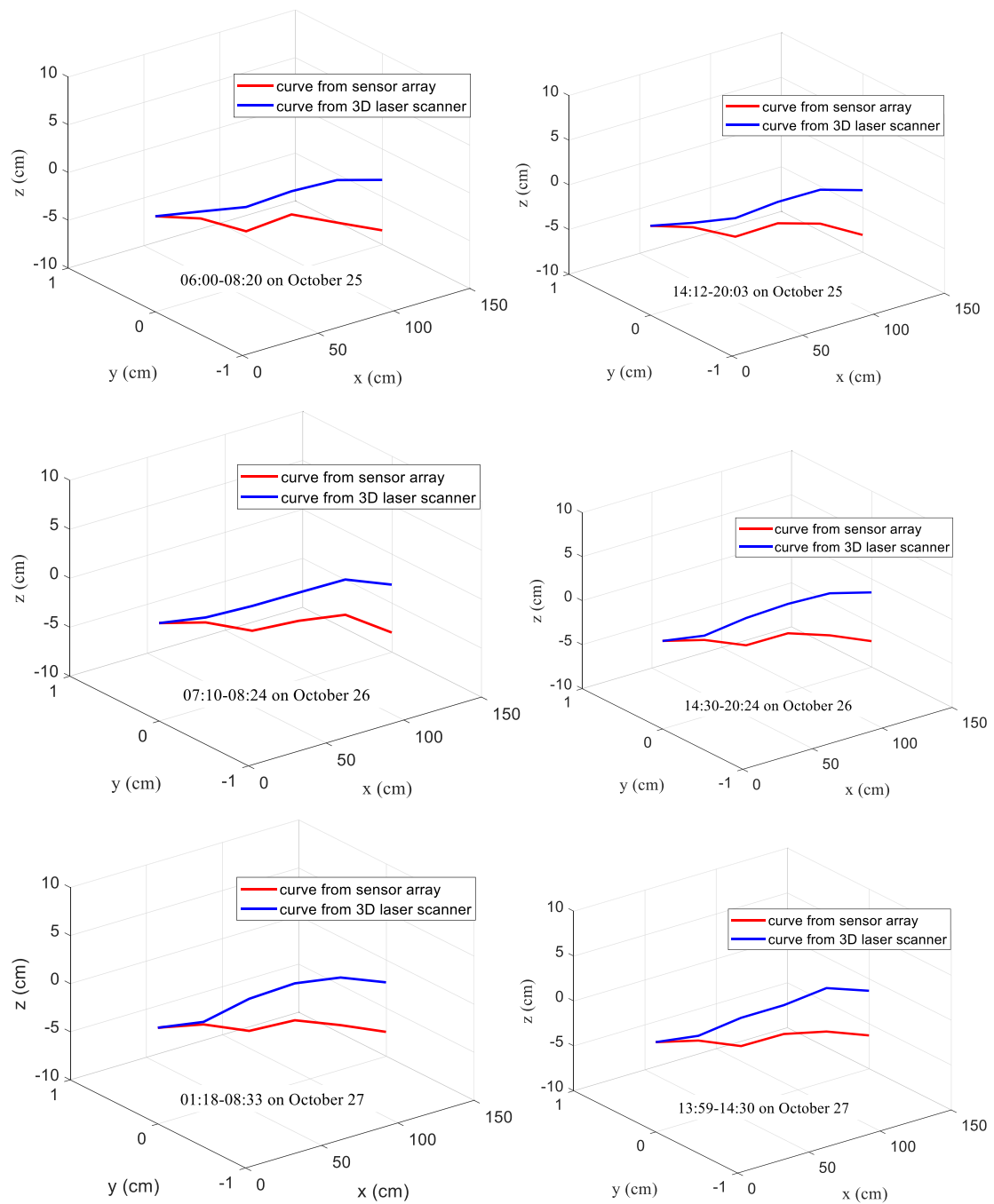


Fig. 10. Curves obtained from the sensor array and 3D laser scanner.

Table 2

Coordinate errors between the sensor array and 3D laser scanner.

Time	Root mean square error (cm)	Mean absolute error (cm)	Maximum absolute error (cm)
06:00–08:20 on October 25	2.07	2.57	5.28
14:12–20:03 on October 25	2.79	2.29	5.01
07:10–08:24 on October 26	2.89	2.40	4.89
14:30–20:24 on October 26	2.24	2.89	5.53
01:18–08:33 on October 27	2.26	2.92	5.14
13:59–14:30 on October 27	2.04	2.83	4.97

Table 3

Coordinate differences of the sensor array and 3D laser scanner.

Time	z-coordinate value of sensor array (cm)	z-coordinate value of 3D laser scanner (cm)
06:00-08:20 on October 25	-1.63	-0.90
	-2.74	-0.94
	0.36	0.25
	-2.26	-0.24
	-2.21	-1.38
14:12-20:03 on October 25	-1.57	-1.07
	-2.46	-0.87
	0.1	0.41
	-1.45	-0.04
	-2.66	-1.92
07:10-08:24 on October 26	-1.33	-0.83
	-2.25	-0.23
	-0.39	-0.04
	-1.80	-0.07
	-2.21	-1.71
14:30-20:24 on October 26	-1.29	-0.8
	-2.01	0.6
	-0.12	0.2
	-1.55	0.2
	-2.06	-1.3
13:59-14:30 on October 27	-1.06	-0.8
	-2.07	1.0
	-0.30	0.2
	-1.91	-0.8
	-2.1	-1.9
14:30-20:24 on October 26	-1.53	-0.7
	-1.72	0.6
	-0.06	0
	-1.12	0.5
	-1.84	-1.7

Author statement

Author Contributions: Chunying Xu and Jiawang chen conceived and designed the experiments; Chunying Xu, Yongqiang Ge, Ziqiang Ren, Chen Cao, Hai Zhu, Yue Huang, Hao Wang, Wei Wang performed the experiments; Chunying Xu and Yongqiang Ge analyzed the data; Chunying Xu wrote the paper.

Declaration of Competing Interest

The authors declare that they have no known competing financial interests or personal relationships that could have appeared to

influence the work reported in this paper.

Acknowledgments

This study is supported by National Key Research and Development Program of China (2017YFC0307703), Guangdong Basic and Applied Basic Research Foundation (2019A1515110372), STU Scientific Research Foundation for Talents (NTF19034), Fundamental Research Funds for the Central Universities (2019XZZX003-05), Special Project for Promoting Economic Development in Guangdong Province with grant NO. GDME-2018D004 and the Key Research and Development Project of Zhejiang Province (2018C03SAA01010).

Table 4

Coordinate difference errors before and after removing the data of sensors #2 and #4.

Time	Before Root mean square error (cm)	Mean absolute error (cm)	Maximum absolute error (cm)	After Root mean square error (cm)	Mean absolute error (cm)	Maximum absolute error (cm)
06:00-08:20 on October 25	2.15	1.10	2.02	0.65	0.33	0.83
14:12-20:03 on October 25	2.04	1.00	1.58	0.90	0.40	0.87
07:10-08:24 on October 26	1.99	0.98	1.83	0.95	0.43	0.96
14:30-20:24 on October 26	0.97	1.19	2.61	0.22	0.52	0.76
13:59-14:30 on October 27	1.20	1.03	3.07	0.16	0.32	0.50
14:30-20:24 on October 26	0.97	0.99	2.32	0.42	0.34	0.83

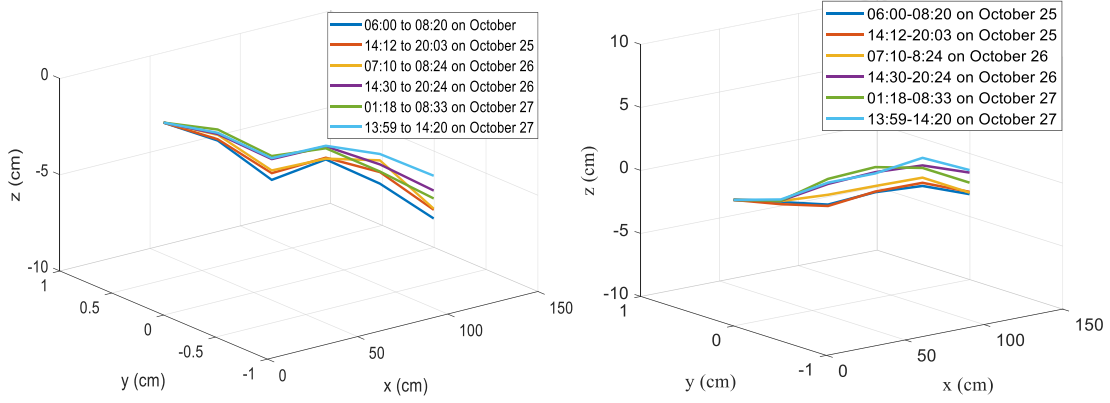


Fig. 11. Tidal flat levels obtained from the (a) sensor array and (b) 3D scanner from October 25 to October 27.

Appendix A. One-dimensional non-uniform sampling theorem

A continuous signal is usually represented and processed by its discrete sampling values $\{f(x_n), n \in \mathbb{Z}\}$, where n is a countable indexing set. In the frames theory, any bandlimited function $f(x)$ can be completely recovered from its sampling values $\{f(x_n), n \in \mathbb{Z}\}$ if the following frame inequality is held:

$$A \|f\|^2 \leq \sum_{n \in \mathbb{Z}} |f(x_n)|^2 \leq B \|f\|^2 \quad (\text{A1})$$

Where A and B are the frame boundaries, and the bandlimited function $f(x) \in PW_\Omega$, the PW_Ω is the *Paley-Wiener space* (bandlimited finite energy signals), defined as:

$$PW_\Omega = \{f(x) \in L^2(\mathbb{R}) : \text{supp } \hat{f} \subseteq [-\Omega, \Omega]\} \quad (\text{A2})$$

Where $L^2(\mathbb{R})$ is the space of the complex-valued finite energy signals defined on the real line \mathbb{R} , \hat{f} is the Fourier transformation of $f(x)$, and $\text{supp } \hat{f}$ is the support of \hat{f} . If $\{e^{j2\pi\Omega x_n}, n \in \mathbb{Z}\}$ is a frame of PW_Ω , the inequality (1) holds, i.e., $f(x)$, can be completely recovered from its sampling values $\{f(x_n), n \in \mathbb{Z}\}$.

In the frames theory, theorem 1 [39,40] states that, if the sampling points $\{x_n, n \in \mathbb{Z}\} \subseteq \mathbb{R}$ are a strictly increasing sequence for which $\lim_{n \rightarrow \pm\infty} x_n = \pm\infty$, and $\exists d, T$ and $\Omega > 0$, such that $0 < d \leq \inf(x_{n+1} - x_n) \leq \sup(x_{n+1} - x_n) = T < \infty$ and $2T\Omega < 1$, then $\{e^{j2\pi\Omega x_n}, n \in \mathbb{Z}\}$ is a frame of PW_Ω . Frame boundaries A and B satisfy inequalities $A \geq \frac{(1-2T\Omega)^2}{T}$ and $B \leq \frac{4}{\pi^2\Omega^2}(e^{\pi\Omega d} - 1)$.

Appendix B. Amplitude spectrum of the tidal flat in Zhairuoshan island

The one-dimensional Fourier transformation of tidal flat for each y value is:

$$F(u, y) = \sum_{x=0}^{M-1} f(x, y) e^{-j2\pi(ux/M)} \quad (\text{A3})$$

Where $f(x, y)$ are the points of the tidal flat, M is the number of samples, and u is a discrete variable equal to $u = 0, 1, 2, \dots, M-1$.

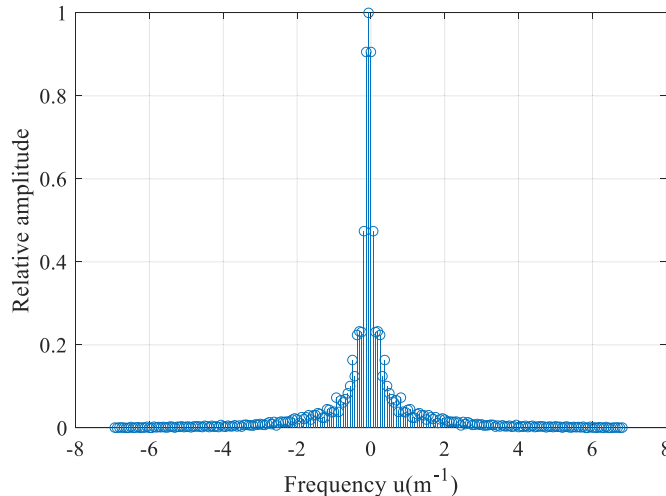


Fig. A1. One-dimensional relative amplitude spectrum at $y = 0.5$ m (after normalization and centralization).

Table A1

One-dimensional highest frequency of the tidal flat.

y (m)	0.5	1	1.5	2	2.5	3	3.5	4
Highest frequency (m-1)	0.375	0.25	0.3125	0.125	0.25	0.125	0.125	0.125
y (m)	4.5	5	5.5	6	6.5	7	7.5	8
Highest frequency (m-1)	0.125	0.125	0.125	0.125	0.0625	0.0625	0.0625	0.25

A total of 160 samples were collected in the x-axis direction. The sampling frequency was $f_s = 160/16 \text{ m} = 10 \text{ m}^{-1}$. The one-dimensional discrete Fourier transformation $F(u, y)$ of the tidal flat was calculated using formula (3), and its amplitude $|F(u, y)|$ was obtained. Fig. A1 shows the one-dimensional relative amplitude spectrum (after normalization and centralization) at $y = 0.5 \text{ m}$. The Fig. A1 shows that the frequency of the tidal flat was generally low and the relative amplitude of the high-frequency spectrum was close to, but not equal to zero. Therefore, we defined the bandwidth (effective bandwidth) of the tidal flat as follows: the frequency range of the 95% energy concentration for the tidal flat. According to Parseval's theorem [41], the total energy of a spatial domain is equal to the total energy of the frequency domain. The minimum frequency when the frequency domain energy reached 95% of the total energy was the bandwidth of the tidal flat, which was the highest frequency of the tidal flat. Table A1 shows the one-dimensional highest frequency of the tidal flat when the sampling interval was 0.1 m . The one-dimensional highest frequency of the tidal flat was 0.375 m^{-1} .

Appendix C. Arrangement conditions of the sensor array

If the slope of the tidal flat is less than 90° , the sampling point set $\{x_n, n = 1, 2, \dots, N\}$ is a strictly increasing sequence, i.e., inequation $x_{n+1} - x_n > 0$ holds for all n . Second, the survey area of the tidal flat was limited, therefore, $\lim_{n \rightarrow \pm\infty} x_n < \infty$. According to theorem 1, we must extend the sampling point $\{x_n, n = 1, 2, \dots, N\}$ and value $\{f(x_n), n = 1, 2, \dots, N\}$ sets to $\{\tilde{x}_n, n = -\infty, \dots, 1, 2, \dots, \infty\}$ and $\{f(\tilde{x}_n), n = -\infty, \dots, 1, 2, \dots, \infty\}$, respectively. The contents were as follows: first, the sampling point set must be a strictly increasing sequence. Set $\tilde{x}_{n+1} - \tilde{x}_n = C$ when $n < 1$ and $n > N$, where C is a constant that must be smaller than $\frac{1}{2\Omega}$ and larger than zero. In this study, we took it as $\frac{1}{3\Omega}$. $\tilde{x}_{n+1} - \tilde{x}_n = x_{n+1} - x_n > 0$ was set when $n = 1, 2, \dots, N$. Second, the extended sample values were set as zeros and the original sample values were kept unchanged. $f(\tilde{x}_n) = 0$ was set when $n < 1$ and $n > N$. $f(\tilde{x}_n) = f(x_n)$ was set when $n = 1, 2, \dots, N$. The new sample set is shown in formulae (A4) and (A5).

$$\tilde{x}_n = \begin{cases} x_1 - \frac{1}{3\Omega}(1 - n), & n = -\infty, \dots, 0 \\ x_n, & n = 1, \dots, N \\ x_N + \frac{1}{3\Omega}(n - N), & n = N + 1, \dots, \infty \end{cases} \quad (\text{A4})$$

$$f(\tilde{x}_n) = \begin{cases} 0, & n = -\infty, \dots, 0 \\ f(x_n), & n = 1, \dots, N \\ 0, & n = N + 1, \dots, \infty \end{cases} \quad (\text{A5})$$

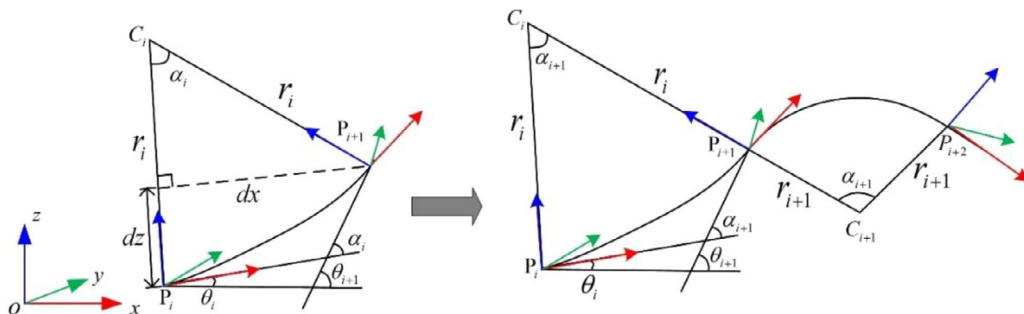
As shown in formulae (4) and (5), the new sampling point set $\{\tilde{x}_n, n = -\infty, \dots, 1, 2, \dots, \infty\}$ meets the conditions of a strict increase and $\lim_{n \rightarrow \pm\infty} \tilde{x}_n = \pm\infty$. Moreover, when the interval between the sensors was smaller than $\frac{1}{2\Omega}$, the maximum distance between the sampling points was smaller than $\frac{1}{2\Omega}$, therefore, $\sup(\tilde{x}_{n+1} - \tilde{x}_n) = T < \frac{1}{2\Omega} < \infty$. A positive constant d (approaching to zero) to meet the condition of $0 < d \leq \inf(\tilde{x}_{n+1} - \tilde{x}_n)$ can always be found. That is, $0 < d \leq \inf(\tilde{x}_{n+1} - \tilde{x}_n) \leq \sup(\tilde{x}_{n+1} - \tilde{x}_n) = T < \infty$ and $2T\Omega < 2 \cdot \frac{1}{2\Omega} \cdot \Omega = 1$. The non-uniform sample set could completely recover the tidal flat when the interval between the sensors was smaller than $\frac{1}{2\Omega}$.

Note that the above process is based on the assumption that there is only one sample point in the range $((n-1)\frac{1}{2\Omega}, n\frac{1}{2\Omega})$, $n = 1, 2, 3, \dots, N$. When the number of sample points in the range is more than one, the sample set can satisfy the theorem 1.

The one-dimensional highest frequency of the tidal flat is 0.375 m^{-1} , which means $\Omega = 0.375 \text{ m}^{-1}$. Thus, according to the derivation process, the interval between the sensors is smaller than $\frac{1}{2\Omega} \approx 1.33 \text{ m}$.

Appendix D. Two-dimensional arc reconstruction algorithm

The shape between the sensors could be approximated by an arc. To resolve the arc, we only needed to know its radius, the coordinates of the center of the circle, and the coordinates of the starting point to determine the coordinates of the end-point.

**Fig. A2.** Schematic diagram of the two-dimensional arc model.

As shown in Fig. A2, α_i is the central angle of arc P_iP_{i+1} , which can be obtained by formula (A6):

$$\alpha_i = \theta_{i+1} - \theta_i \quad (\text{A6})$$

where θ_i is the angle of the i^{th} sensor rotating around the y-axis (pitch of the Euler angle). The angle was determined to be positive in accordance with the right-hand principle, and could be obtained by the three-axis acceleration value of the accelerometer, as shown in formula (A7):

$$\theta_i = \arcsin\left(\frac{-a_x}{\sqrt{a_x^2 + a_y^2 + a_z^2}}\right) \quad (\text{A7})$$

The radius of the arc r_i could then be obtained (A8):

$$r_i = l / \alpha_i \quad (\text{A8})$$

where l is the arc length between two sensors. The coordinate of point P_{i+1} in coordinate system $P_i x_i y_i z_i$ (P_i is the origin) is:

$$P_{i+1}^i = [dx, 0, dz]^T = \begin{cases} [r_i \sin(\alpha_i), 0, -(r_i - r_i \cos(\alpha_i))]^T, & \alpha_i > 0 \\ [l, 0, 0]^T, & \alpha_i = 0 \\ [-r_i \sin(\alpha_i), 0, r_i - r_i \cos(\alpha_i)]^T, & \alpha_i < 0 \end{cases} \quad (\text{A9})$$

The coordinate of point P_{i+1} in the coordinate system $oxyz$ (o is the origin) is then:

$$\begin{bmatrix} P_{i+1}^0 \\ 1 \end{bmatrix} = H_i^0 \begin{bmatrix} P_{i+1}^i \\ 1 \end{bmatrix} = \begin{bmatrix} R_i^0 & P_i^0 \\ O_3^T & 1 \end{bmatrix} \begin{bmatrix} P_{i+1}^i \\ 1 \end{bmatrix} \quad (\text{A10})$$

where R_i^0 is the rotation matrix from coordinate system $P_i x_i y_i z_i$ to coordinate system $oxyz$, which is $R_i^0 = R_{i-1}^0 R_i^{i-1}$. R_i^0 is a unit matrix when $i = 1$. Matrix R_i^{i-1} was obtained from formula (A11). The x-axis direction of coordinate system $P_{i+1} x_{i+1} y_{i+1} z_{i+1}$ could be obtained from coordinate system $P_i x_i y_i z_i$ after rotation around the y_i -axis with angle α_i .

$$R_i^{i-1} = \begin{bmatrix} \cos(\alpha_i) & 0 & \sin(\alpha_i) \\ 0 & 1 & 0 \\ -\sin(\alpha_i) & 0 & \cos(\alpha_i) \end{bmatrix} \quad (\text{A11})$$

References

- J.Y. Chen, H.Q. Cheng, Z.J. Dai, D. Eisma, Harmonious development of utilization and protection of tidal flats and wetlands - a case study in Shanghai area, China Ocean Eng. 22 (2008) 649–662.
- K.H. Tseng, C.Y. Kuo, T.H. Lin, Z.C. Huang, Y.C. Lin, W.H. Liao, et al., Reconstruction of time-varying tidal flat topography using optical remote sensing imagery, ISPRS J. Photogramm. Remote Sens. 131 (2017) 92–103.
- M.L. Stutz, O.H. Pilkey, Global distribution and morphology of deltaic barrier island systems, J. Coastal Res. 36 (1) (2002) 694–707.
- C. Choi, D.J. Kim, Optimum baseline of a single-pass in-sar system to generate the best DEM in tidal flats, IEEE J. Select. Topics Appl. Earth Observ. Remote Sens. (2018) 1–11.
- K. Reise, Tidal Flat Ecology: An Experimental Approach to Species Interactions 54 Springer, New York, NY, USA, 2012.
- M.L. Parry, Climate Change 2007-Impacts, Adaptation and Vulnerability: Working Group II Contribution to the Fourth Assessment Report of the IPCC 4 Cambridge Univ. Press, Cambridge, U.K., 2007.
- M. Finlayson, R.D. Cruz, N. Davidson, et al., Millennium ecosystem assessment: ecosystems and human well-being: wetlands and water synthesis, Data Fusion Concepts Ideas 656 (1) (2005) 87–98.
- A. Lemke, M. Lunau, J. Stone, O. Dellwig, M. Simon, Spatiotemporal dynamics of suspended matter properties and bacterial communities in the back-barrier tidal flat system of Spiekeroog Island, Ocean Dyn. 59 (2009) 277–290.
- M.L. Kirwan, J.P. Megonigal, Tidal wetland stability in the face of human impacts and sea-level rise, Nature 504 (2013) 53–60.
- H.T.C. Van Stokkom, G.N.M. Stokman, J.W. Hovenier, Quantitative use of passive optical remote sensing over coastal and inland water bodies, Int. J. Remote Sens. 14 (3) (1993) 541–563.
- B.H. Choe, D.J. Kim, J.H. Hwang, et al., Detection of oyster habitat in tidal flats using multi-frequency polarimetric SAR data, Estuarine Coastal Shelf Sci. 97 (2012) 28–37.
- R. Aedla, G.S. Dwarakish, D.V. Reddy, Automatic shoreline detection and change detection analysis of netravati-gurpur river mouth using histogram equalization and adaptive thresholding techniques, Aquatic Procedia 4 (2015) 563–570.
- B. Wessel, M. Huber, C. Wohlfart, U. Marschall, D. Kosmann, A. Roth, Accuracy assessment of the global tandem-X digital elevation model with GPS data, ISPRS J. Photogramm. Remote Sens. 139 (2018) 171–182.
- Y.X. Liu, M.C. Li, L. Mao, L. Cheng, F.X. Li, Toward a method of constructing tidal flat digital elevation models with medium and medium-resolution satellite images, J. Coastal Res. 29 (2) (2013) 438–448.
- S.K. Lee, J.H. Ryu, High-accuracy tidal flat digital elevation model construction using tandem-X science phase data, IEEE J. Select. Topics Appl. Earth Observ. Remote Sens. 10 (6) (2017) 2713–2724.
- S. Coveney, X. Monteys, Integration potential of infomar airborne lidar bathymetry with external onshore lidar data sets, J. Coastal Res. 62 (2011) 19–29.
- Q. Li, X. Ding, A. Zhu, L. Cheng, Y. Kang, T. Zhang, Neural network modeling of tidal flat terrain based on lidar survey data, Proc Spie 8286 (4) (2011) 209–224.
- A. Campbell, Y. Wang, Examining the influence of tidal stage on salt marsh mapping using high-spatial-resolution satellite remote sensing and topobathymetric lidar, IEEE Trans. Geosci. Remote Sens. (2018) 1–8.
- H.F. Stockdon, A.H. Sallenger, J.H. List, R.A. Holman, Estimation of shoreline position and change using airborne topographic lidar data, J. Coastal Res. 18 (2002) 502–513.
- Y. Liu, H. Huang, Z. Qiu, J. Fan, Detecting coastline change from satellite images based on beach slope estimation in a tidal flat, Int. J. Appl. Earth Obs. Geoinf. 23 (Complete) (2013) 165–176.
- Z. Xu, D.J. Kim, S.H. Kim, Y.-K. Cho, S.-G. Lee, Estimation of seasonal topographic variation in tidal flats using waterline method: a case study in Gomso and Hampyeong Bay, South Korea, Estuarine, Coastal Shelf Sci. 183 (2016) 213–220.
- G. Heygster, J. Dannenberg, J. Notholt, Topographic mapping of the German tidal flats analyzing SAR images with the waterline method, IEEE Trans. Geosci. Remote Sens. 48 (3) (2010) 1019–1030.
- J.H. Ryu, J.S. Won, K.D. Min, Waterline extraction from Landsat TM data in a tidal flat—A case study in Gomso Bay, Korea, Remote Sens. Environ. 83 (2002) 442–456.
- M. Potouroglou, J.C. Bull, K.W. Krauss, et al., Measuring the role of seagrasses in regulating sediment surface elevation, Sci Rep 7 (1) (2017) 1–11.
- S.S. Rumrill, D.C. Sowers, Concurrent assessment of eelgrass beds (*Zostera marina*) and salt marsh communities along the estuarine gradient of the South Slough, Oregon, J. Coastal Res. (2008) 121–134.
- C. Marion, E.J. Anthony, A. Trentesaux, Short-term (≤ 2 yrs) estuarine mudflat and saltmarsh sedimentation: high-resolution data from ultrasonic altimetry, rod surface-elevation table, and filter traps, Estuar. Coast. Shelf Sci. 83 (4) (2009) 475–484.
- K. Tan, J. Chen, W. Qian, et al., Intensity Data Correction for Long-Range Terrestrial Laser Scanners: a Case Study of Target Differentiation in an Intertidal Zone, Remote Sens. 11 (3) (2019) 331.
- W. Xie, Q. He, K. Zhang, et al., Application of terrestrial laser scanner on tidal flat morphology at a typhoon event timescale, Geomorphology 292 (2017) 47–58.
- R. Gens, Remote sensing of coastlines: detection, extraction and monitoring, Int. J. Remote Sens. 31 (2010) 1819–1836.
- E.H. Boak, I.L. Turner, Shoreline definition and detection: a review, J. Coast Res. 21 (2005) 688–703.
- B.L. Cui, X.Y. Li, Coastline change of the Yellow River estuary and its response to the sediment and runoff (1976–2005), Geomorphology 127 (2011) 32–40.
- N.D. Ahearn, J.Y. Takekawa, B. Jaffe, B.J. Hattenbach, A.C. Foxgrover, Mapping elevations of tidal wetland restoration sites in San Francisco Bay: comparing accuracy of aerial lidar with a singlebeam echosounder, J. Coastal Res. (2010) 312–319.

- [33] D.R. Cahoon, J.C. Lynch, B.C. Perez, et al., High-precision measurements of wetland sediment elevation: II. The rod surface elevation table, *J. Sediment. Res.* 72 (5) (2002) 734–739.
- [34] C. Xu, J. Chen, H. Zhu, H. Liu, Y. Lin, Experimental research on seafloor mapping and vertical deformation monitoring for gas hydrate zone using nine-axis mems sensor tapes, *IEEE J. Oceanic Eng.* (2018) 1–12.
- [35] C. Xu, J. Chen, H. Zhu, P. Zhang, Z. Ren, H. Zhu, et al., Design and laboratory testing of a MEMS accelerometer array for subsidence monitoring, *Rev. Sci. Instrum.* 89 (8) (2018) 085103-1-085103-6.
- [36] C. Xu, J. Chen, H. Zhu, et al., Experimental Study on Seafloor Vertical Deformation Monitoring Based on MEMS Accelerometer Array, *Proc of the 28th International Ocean and Polar Engineering Conference, Japan, ISOPE, 2018*, www.isopec.org.
- [37] H. Zhu, C. Xu, J. Chen, et al., Research on distributed synchronous acquisition system for seabed terrain deformation monitoring, *Oceans, IEEE*, 2018.
- [38] X. Zhang, D. Pan, J. Chen, et al., Evaluation of coastline changes under human intervention using multi-temporal high-resolution images: a case study of the Zhoushan Islands, China, *Remote Sens.* 6 (10) (2014) 9930–9950.
- [39] J.J. Benedetto, Irregular sampling and frames, in: C.K. Chui (Ed.), *Wavelets: A Tutorial in Theory and Applications*, Academic Press, Boston, 1992, pp. 445–507.
- [40] F. Marvasti, *Nonuniform Sampling: Theory and Practice*, Kluwer Academic/Plenum Publishers, New York, 2001.
- [41] Haykin, S., and Veen, B.V., 2003. *Signals and systems*. Pub. House of Electronic.